DOI: 10.1002/((please add manuscript number))
Article type: Communication

Tunable Modal Birefringence in Low-loss van der Waals Waveguide

Debo Hu, Ke Chen, Xinzhong Chen, Xiangdong Guo, Mengkun Liu, and Qing Dai**

Dr. D. B. Hu, K. Chen, X. D. Guo, Prof. Q. Dai
Division of Nanophotonics, CAS Center for Excellence in Nanoscience, National Center for Nanoscience and Technology, Beijing 100190, China
E-mail: daiq@nanoctr.cn
X. Z. Chen, Prof. M. K. Liu
Department of Physics, Stony Brook University, Stony Brook, NY 11794, USA
E-mail: mengkun.liu@stonybrook.edu

Keywords: optical anisotropy, phase retardation, planar waveguide, polarization management, near-field imaging

Abstract: van der Waals (vdW) crystals are promising candidates for integrated phase retardation applications due to their large optical birefringence. Among the two major types of vdW materials, the hyperbolic vdW crystals are inherently inadequate for optical retardation applications since the supported polaritonic modes are exclusively transverse-magnetic (TM) polarized and relatively lossy. Elliptic vdW crystals, on the other hand, represent a superior choice. For example, molybdenum disulfide (MoS_2) is a natural uniaxial vdW crystal with extreme elliptic anisotropy in the frequency range of optical communication. Both transverse-electric (TE) polarized ordinary and TM polarized extraordinary waveguide modes can be supported in MoS_2 microcrystals with suitable thicknesses. In this work, low-loss transmission of these guided modes is demonstrated with nano-optical imaging at the near-infrared (NIR) wavelength (1530 nm). More importantly, by combining theoretical calculations and NIR nanoimaging, the modal birefringence between the orthogonally polarized TE and TM modes is shown to be tunable in both sign and magnitude via varying the thickness of the MoS_2 microcrystal. This tunability represents a unique new opportunity to control the polarization behavior of photons with vdW materials.

Phase retardation elements such as waveplates and compensators are important polarization management components that play an essential part in modern optical communication systems.[1,2] Anisotropic crystals exhibiting optical birefringence are the fundamental building blocks of these bulk components.[3,4] With the advancement of nano-optics in the quantum era, miniaturization and integration of these phase retardation components become imperative.[5-7] In analogy with their bulk counterparts which introduce path difference between orthogonally polarized light through optical birefringence, the integrated optical phase retardation elements import path difference between orthogonally polarized guided modes via the modal birefringence of the waveguides.[8] Unlike the bulk birefringence which is predefined by the material, the modal birefringence of waveguides are tunable with constituent materials and waveguide geometry.[9] However in practice the manufacture of integrated phase retarders with designed modal birefringence is particularly challenging because of their stringent fabrication tolerance.[10] Therefore, new materials allowing layer-by-layer control and fine mechanical processing are highly demanded.

Due to the difference between their interlayer and intralayer bonding strengths, van der Waals (vdW) crystals are both mechanically and optically anisotropic.[11,12] In light of this intrinsic out-of-plane bi-anisotropy, vdW crystals are promising materials for the phase retardation applications in integrated optical circuits: the mechanical anisotropy permits the precise layer-by-layer manufacturing of the waveguide structure while the optical anisotropy provides one more degree of freedom to control its modal birefringence. vdW crystals with hyperbolic optical responses such as hexagonal boron nitride (*h*-BN)[13,14] and α-phase molybdenum trioxide (α-MoO_3)[15,16] have been demonstrated to support highly confined phonon polaritons in the mid-infrared (MIR) frequency range. However, these polaritonic modes are inherently inadequate for the integrated phase retardation applications (polariton-assisted polarization control of far-field light with metasurfaces made of vdW materials is possible[17]), as a result of their inevitable transmission loss (imposed by the Kramers-Kronig relationships between dispersion and dissipation[18,19]) and the absence of transverse-electric (TE) polarized modes.[20,21] An alternative way is to resort to vdW crystals with elliptic anisotropy at

frequencies far away from any resonant absorption bands. In such case, the imaginary parts of the permittivity tensor are usually negligible and result in positive real parts.[22] The near-zero imaginary parts of permittivity guarantee the low-loss transmission of the supported waveguide modes, while the positive real parts allow the co-occurrence of TE and transverse-magnetic (TM) polarized modes. Transition metal dichalcogenides (TMDs) are expected to exhibit elliptic light dispersion in a broad frequency range (note that *h*-BN is also elliptically anisotropic out of its Reststrahlen bands, the reason TMDs are better for our proposed applications will be discussed at a later stage);[23] this elliptic anisotropy together with the single-layer precisely modifiable structure[24,25] of TMDs would permit fine-tuning of the modal birefringence between TE and TM polarized modes, and thus enable the implementation of phase retarders in integrated optical circuits.

In this work, we choose molybdenum disulfide (MoS_2)[26-29] as a representative for TMDs to introduce the concept of vdW optical phase retarders. We first show the low-loss transmission of waveguide modes in MoS_2 in the near-infrared (NIR) frequency range by comparing the near-field imaging results between MoS_2 and *h*-BN at the same excitation wavelength λ=1530 nm. We then demonstrate that the modal birefringence between the orthogonally polarized ordinary (TE) and extraordinary (TM) guided modes can be fine-tuned by varying the thickness of the MoS_2 crystal, as a result of its extreme out-of-plane elliptic anisotropy (the optical birefringence of MoS_2 at 1530 nm is about 1.4,[30] much larger than those of common non-vdW crystals and the state-of-the-art barium titanium sulfide[31,32]). Functionalities of the proposed vdW zero-order half-wave plates and phase-matched waveguide will also be discussed via numerical simulations.

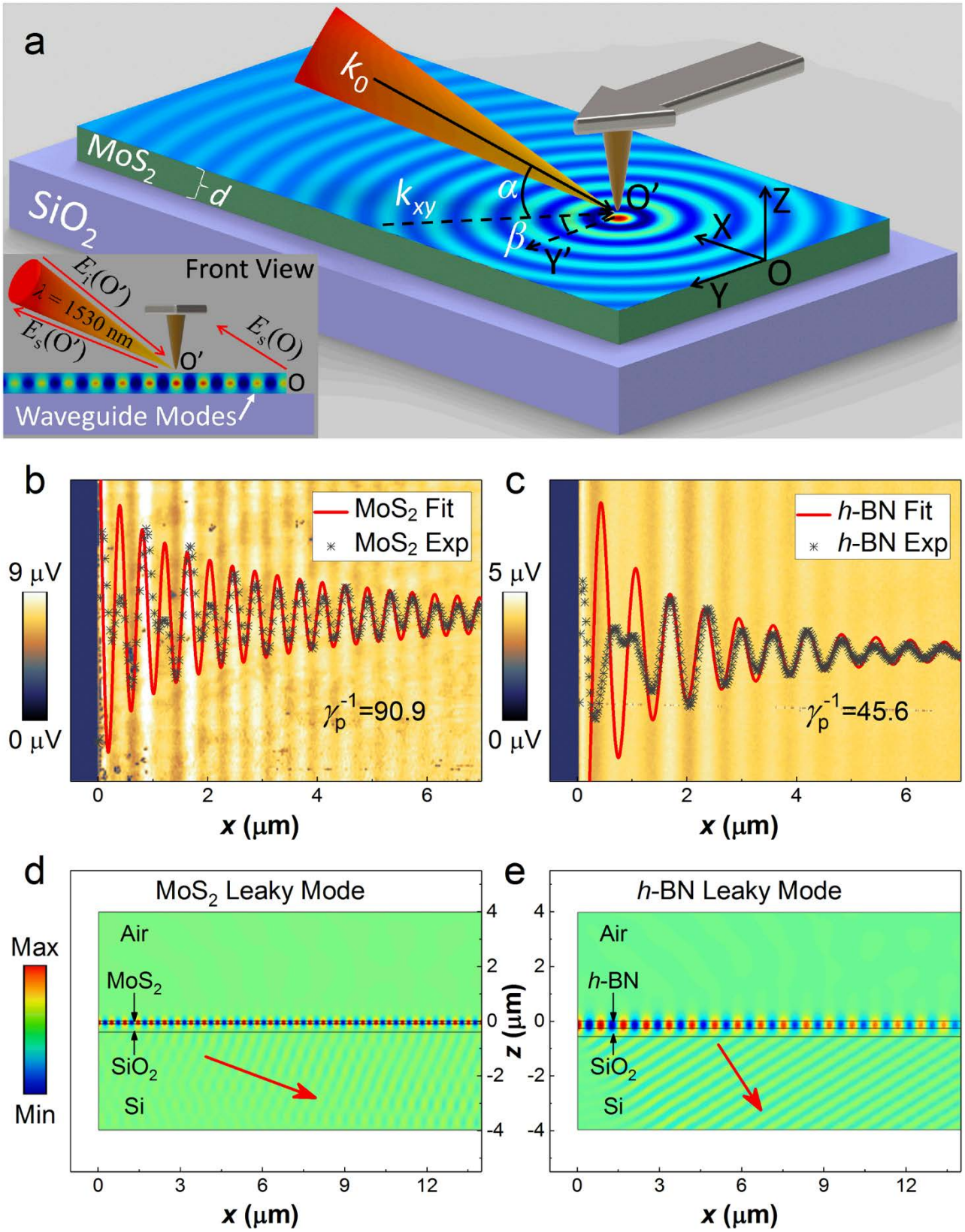

Figure 1. Optical nanoimaging of the waveguide modes in MoS_2 and *h*-BN. a) Experimental setup for MoS_2 NIR nanoimaging. The sharp edges of MoS_2 microcrystals are aligned to the *y* axis and the s-SNOM tip scans along the *x* axis. α is the angle between the illumination wavevector k_0 and its projection in the *x*-*y* plane k_{xy}, β is the angle between k_{xy} and the investigated sample edge. Inset is the front view of the experimental setup, the tip-launched guided modes are scattered into free space at the sample edge and interfere with the tip-scattered light at the photodetector. b) and c) NIR nanoimaging results for a 110-nm-thick MoS_2 and a 270-nm-thick *h*-BN microcrystals at the same

excitation wavelength λ=1530 nm, respectively. The inverse damping ratios γ_p^{-1} of the guided modes can be obtained by fitting the fringe profiles with damped cosine waves. Note that the first three experimentally obtained fringes have been left out in the fitting procedure in both b and c, to eliminate the interference from the edge-launched guided modes. d) and e) Numerical simulations of the mode propagation in MoS_2 and *h*-BN, respectively. Due to the finite thickness of the SiO_2 layer, the guided modes can leak out of the waveguides and lead to the observed transmission losses in b and c. Moreover, due to the lower field confinement, the guided modes in *h*-BN tunnel through the SiO_2 layer much easier than those in MoS_2, thus suffering higher transmission loss. The red arrows indicate the propagation directions of the leaked light in Si. Note that for *h*-BN the mode leakage rate is higher than that for MoS_2.

Near-field optical images of the waveguide modes in MoS_2 and *h*-BN were obtained by scattering-type scanning near-field optical microscopy (s-SNOM).[33-37] (see Experimental Section). **Figure 1**a is the schematic diagram of the experimental setup for MoS_2 NIR nanoimaging. The MoS_2 microcrystal is exfoliated onto standard silicon wafer with a 300-nm-thick SiO_2 top layer. The laser beam with a wavelength of 1530 nm is focused onto the apex of the s-SNOM tip to excite both ordinary and extraordinary guided modes in the air-MoS_2-SiO_2 three-layer waveguide. These modes spread circularly in the waveguide until they come across the sharp edge of the MoS_2 microcrystal. At the edge, part of these guided modes get scattered into the far field and interfere with the tip-scattered light at the photodetector (inset of Figure 1a). With the sample raster-scanning under the s-SNOM tip, an interference pattern can therefore be recorded. Since their paths back to the photodetector are both oblique to the MoS_2 surface, the optical path difference between the tip-scattered and the edge-scattered light depends on the direction of the MoS_2 edge, and therefore the s-SNOM images of the guided modes are strongly edge-orientation dependent. To reduce the complexity in data analysis, we align the edge of MoS_2 vertically along the direction of the AFM cantilever and scan horizontally. In this way, the obtained apparent effective indices of refraction for the guided modes differentiate from the genuine ones only by a constant geometrical factor $\cos\alpha \sin\beta$ (α is the angle between the illumination wavevector k_0 and its projection in the x-y plane k_{xy}, β is the angle between k_{xy} and the investigated sample edge).[30,38] To compare the transmission losses of the guided modes in MoS_2 and *h*-BN, we repeated the same experiment on *h*-BN using the same setup.

Experimental results for the near-field imaging of a 110-nm-thick MoS_2 and a 270-nm-thick *h*-BN microcrystals are compared side by side in Figure 1b and c. It is obvious to see that the waveguide mode in MoS_2 exhibits a relatively higher wavelength compression and a much longer propagation distance than that in *h*-BN. To quantify the transmission losses of the guided modes, we fit the experimental data with a damped cosine wave

$$s(x) = A\cos(q_1 x + B)\frac{\exp(-q_2 x)}{x^{\eta}} + C. \qquad (1)$$

In **Equation 1** $s(x)$ is the magnitude of the near-field signal, A is the amplitude of cosine wave, B is a phase constant, C is the DC component of near-field signal, q_1 is the apparent wavevector of waveguide modes, q_2 is the damping factor, and η is a factor accounting for the circular spreading of tip-launched waveguide modes. The fitted curves are overlaid to the near-field fringes in Figure 1b and c. The inverse damping ratio $\gamma_p^{-1}=q_1/q_2$ is 90.9 for MoS_2 and 45.6 for *h*-BN. This disparity in transmission loss is counter-intuitive at the first glance since both MoS_2 and *h*-BN are dielectric media at the wavelength of 1530 nm and thus only minor scattering loss from the fabrication imperfection is expected. However, the experimental results can be understood if we take the finite layer thickness (300 nm) of SiO_2 into consideration and regard both the MoS_2 and the *h*-BN heterostructures as leaky mode waveguides,[39] in which all the guided modes with effective indices of refraction less than the refractive index of Si (3.5) tend to tunnel through the SiO_2 layer and dissipate in the Si layer below. The guided modes are better confined in MoS_2 in both vertical and horizontal directions as a result of its relatively higher refractive indices than those of *h*-BN,[30] as demonstrated by numerical simulations in Figure 1d and e. This better vertical confinement makes the guided modes in MoS_2 less likely to leak out and therefore exhibit lower loss in practice.

Of course, the low transmission loss alone does not necessarily make TMDs of unique appeal in integrated optical phase retardation applications; it is the extreme elliptic anisotropy in the technologically important NIR frequency range that holds the key. In isotropic materials, different guided modes are forbidden from possessing the same effective index of refraction by the optical

nondegeneracy theorem (see Section 1 in the Supporting Information for details). Therefore, phase matching between different guided modes in this kind of waveguide can never be achieved and the modal birefringence is only tunable in magnitude in a limited range.[40] On the contrary, the nondegeneracy between orthogonally polarized guided modes can be violated in a planar waveguide comprising elliptically anisotropic media (see Section 2 in the Supporting Information for details) and the modal birefringence is tunable in both sign and magnitude in a wide range. In the following, to theoretically investigate the modal birefringence tunability of vdW waveguides, we take MoS_2 and *h*-BN as representative examples again.

The characteristic equations for the TE and TM polarized guided modes in a planar waveguide made of uniaxially anisotropic guiding layer and isotropic cladding layers can be written as[30]

$$k_0\sqrt{n_o^2-n_{\text{eff,TE}}^2}\,d=\tan^{-1}\left(\frac{\sqrt{n_{\text{eff,TE}}^2-n_1^2}}{\sqrt{n_o^2-n_{\text{eff,TE}}^2}}\right)+\tan^{-1}\left(\frac{\sqrt{n_{\text{eff,TE}}^2-n_2^2}}{\sqrt{n_o^2-n_{\text{eff,TE}}^2}}\right)+p\pi \quad (2)$$

and

$$k_0\frac{n_o}{n_e}\sqrt{n_e^2-n_{\text{eff,TM}}^2}\,d=\tan^{-1}\left(\frac{n_on_e}{n_1^2}\frac{\sqrt{n_{\text{eff,TM}}^2-n_1^2}}{\sqrt{n_e^2-n_{\text{eff,TM}}^2}}\right)+\tan^{-1}\left(\frac{n_on_e}{n_2^2}\frac{\sqrt{n_{\text{eff,TM}}^2-n_2^2}}{\sqrt{n_e^2-n_{\text{eff,TM}}^2}}\right)+q\pi\,, \quad (3)$$

respectively. In **Equation 2** and **3**, k_0 is the free-space wavenumber; d is the guiding layer thickness; n_o and n_e are the ordinary and extraordinary refractive indices of the guiding layer, respectively; n_1 and n_2 are the refractive indices of superstrate and substrate layers, respectively; p and q are the order numbers of TE and TM modes, respectively; $n_{\text{eff,TE}}$ and $n_{\text{eff,TM}}$ are effective indices of refraction for TE and TM modes, respectively. Specifically, Equation 2 and 3 can be reduced to the characteristic equations for guided modes in a planar waveguide made of exclusively isotropic materials by equalizing n_o and n_e.[41]

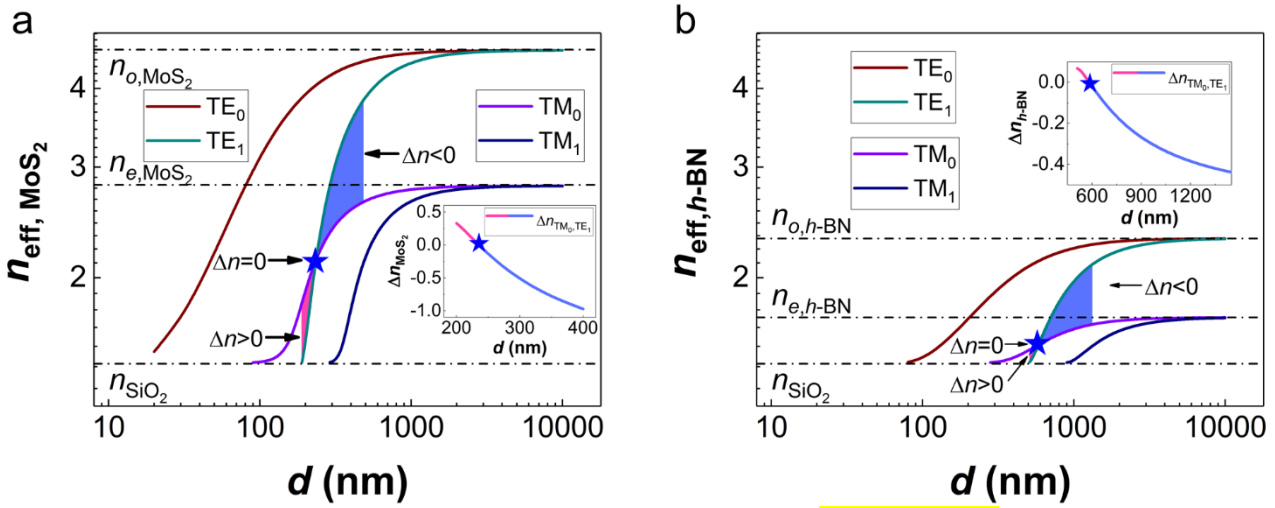

Figure 2. Modal birefringences between orthogonally polarized guided modes in vdW waveguides. a) and b) Thickness dispersions of ordinary and extraordinary modes in the air-MoS_2-SiO_2 and air-*h*-BN-SiO_2 waveguides, respectively. The blue stars indicate the phase matching points of the TM_0 and TE_1 modes in both MoS_2 and *h*-BN waveguides. On the left side of these critical points, the modal birefringence between TM_0 and TE_1 defined as $\Delta n=n_{eff,TM0}-n_{eff,TE1}$ is positive, while on the right side Δn is negative. The insets in a and b show that the modal birefringence in vdW waveguides can be tuned in both sign and magnitude continuously by changing thickness of the guiding layer. The larger the out-of-plane anisotropy the broader the tuning range of the modal birefringence. Note that in both a and b double logarithmic scales are used.

Shown in **Figure 2**a are the thickness dispersions of the four lowest-order guided modes in the air-MoS_2-SiO_2 three-layer waveguide, obtained by solving Equation 2 and 3 numerically. There are two intriguing features demonstrated in Figure 2a: the grouping yet non-crossing of guided modes with the same polarization state, and the crossing of guided modes with different polarization states. Specifically, in the limit of d approaching the cut-off thickness of each guided mode, n_{eff} of the relevant mode approaches the substrate refractive index; as d approaches infinity, n_{eff} for the TM (TE) polarized extraordinary (ordinary) modes approaches asymptotically to the value of n_e (n_o). Since $n_e<n_o$ for MoS_2, the lth order TM mode intersects with all the $\geq l$+1th TE modes. At the intersection point (indicated by a blue star, d=236 nm), the two orthogonal guided modes share the same effective index of refraction, i.e. being phase matched. At this phase matching point, the modal birefringence between TM_0 and TE_1 defined as $\Delta n=n_{eff,TM0}-n_{eff,TE1}$ is exactly zero; while it is positive on the left side of this critical point and negative on the right side. Therefore, the modal birefringence between TM_0 and TE_1 is tunable in both sign and magnitude via varying the thickness of the MoS_2 microcrystal. The guided modes in *h*-BN exhibit similar dispersion behaviors to those in MoS_2, as shown in Figure

2b. However, the tuning range of the resultant modal birefringence is much narrower than that of MoS_2. This is because the maximum tuning range of the modal birefringence is fundamentally limited by the optical anisotropy of the waveguide material: the larger the out-of-plane anisotropy the broader the tuning range of the modal birefringence (this claim can be further confirmed by considering the extreme situation of isotropic guiding layer, i.e. zero material birefringence, see Section 3 in the Supporting Information for details). Since the optical birefringence of *h*-BN is significantly less than that of MoS_2 at the wavelength of 1530 nm,[30] the tunability of the modal birefringence in *h*-BN falls in between the cases of a pure isotropic material and MoS_2. This is another reason why *h*-BN is inferior to MoS_2 for our proposed applications.

To verify the sign and magnitude bi-tunability of modal birefringence between TM_0 and TE_1 modes in the air-MoS_2-SiO_2 waveguide experimentally, we conducted a series of NIR near-field imaging of MoS_2 microcrystals with thicknesses ranging from 205 nm to 360 nm in order to encompass the critical thickness d=236 nm. In **Figure 3**a, we show the fringe profiles of the guided modes in waveguides with different MoS_2 thicknesses (see Section 4 in the Supporting Information for the corresponding near-field images). The indeterminate fringe spacings and the evident beat notes in the near-field profiles strongly indicate the presence of multi-mode superposition, which can be revealed by Fourier analysis of the data in momentum space.[30,38] Figure 3b shows the momentum-space spectra of the fringe profiles in Figure 3a. The geometrical factor in the wavevectors has been corrected by shifting all the spectra to the left by a value of $\cos\alpha\sin\beta$. As assigned in Figure 3b, each peak corresponds to a single guided mode or doubly-degenerate modes, except for the left-most ones, which are assigned to the air mode that originates from the residual far-field interferences.[30,38] All the guided modes shift towards the high spatial frequency direction with the increase of the guiding layer thickness.

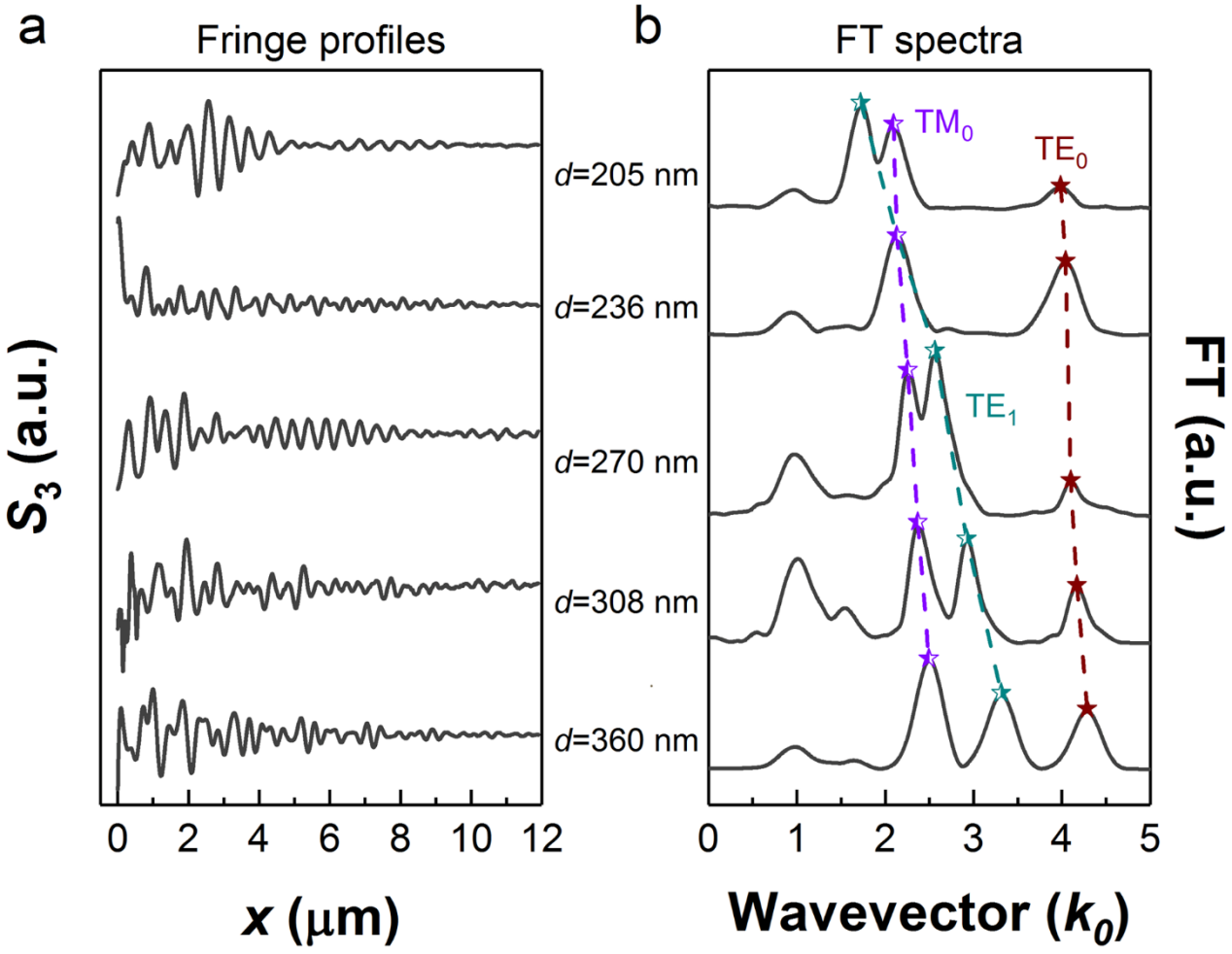

Figure 3. Experimental verification of the sign and magnitude bi-tunability of modal birefringence in the air-MoS_2-SiO_2 three-layer waveguide. a) Fringe profiles of the guided modes corresponding to different MoS_2 thicknesses. b) Momentum-space spectra of the imaged guided modes, obtained by imposing Fourier transform on the near-field fringe profiles in a. The dash lines correspond to the first three dispersion curves in Figure 2a.

The modal birefringence Δn defined above can be experimentally obtained by taking the difference between the peak positions of TM_0 and TE_1. As shown in **Figure 4**a, Δn is initially positive and decreases with the increasing MoS_2 thickness in the range from 205 nm to 360 nm (Δn_{205nm}=+0.30, Δn_{360nm}=-0.82), with the zero-crossing point at a thickness of about 236 nm. At this critical thickness, as the corresponding peaks coincide and merge into a single one in the momentum space (Figure 3b), the TM_0 mode and the TE_1 mode are perfectly phase matched.

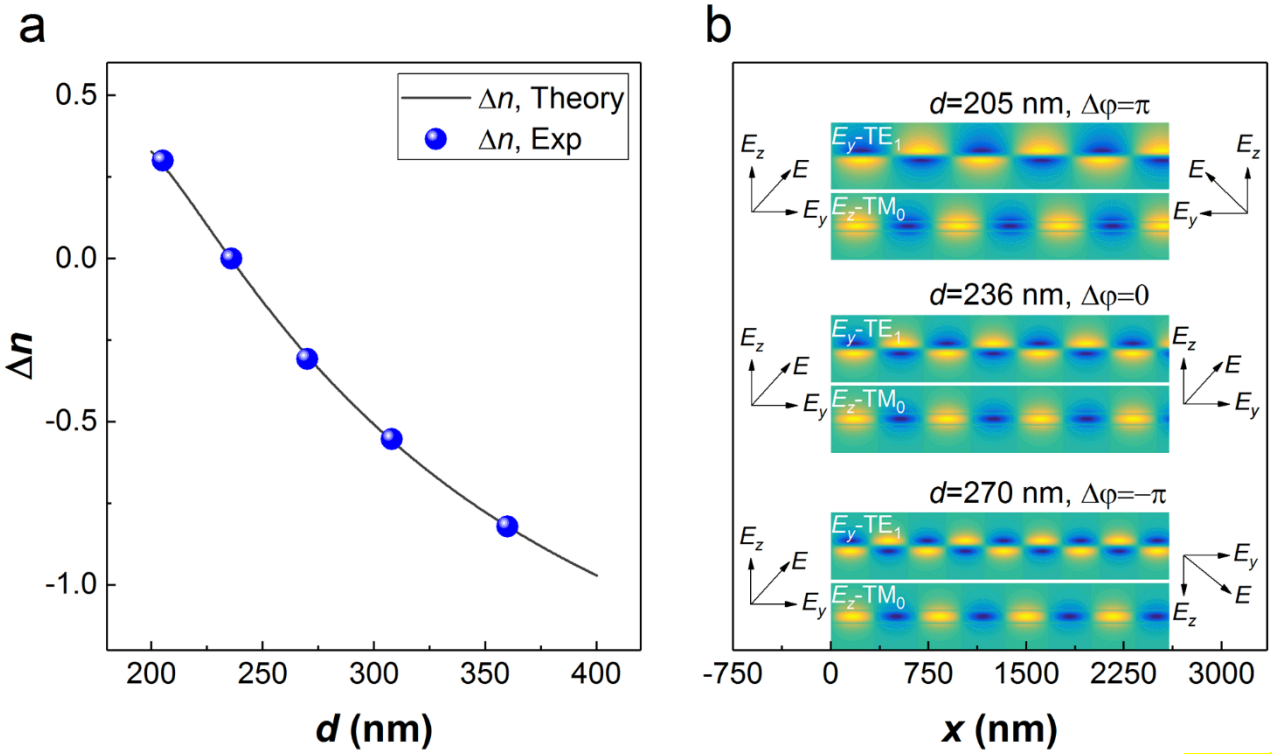

Figure 4. a) Experimentally obtained modal birefringence Δn between the TM_0 and TE_1 guided modes, it can be tuned continuously from positive to negative by varying the guiding layer thickness. The theoretical curve is a duplicate of the inset in Figure 2a. b) Numerical simulations of the real-space electric field distributions associated with TM_0 and TE_1 modes in waveguides with different MoS_2 thicknesses. As a result of the modal birefringence shown in a, the polarization direction of the total field *E* tends to change as the modes propagate along the waveguide: only in the case of perfect phase matching (the middle panel) the polarization direction of *E* can maintain; in the cases of both positive and negative modal birefringences (the upper and lower panels), the polarization direction of *E* always rotates, anticlockwise and clockwise, respectively.

The sign and magnitude bi-tunability of the modal birefringence between orthogonally polarized low-loss guided modes is of special interest in the polarization management in integrated photonic devices. In the case of $\Delta n=0$, phase matching between the TE polarized ordinary and the TM polarized extraordinary modes (middle panel of Figure 4b) allows a new phase-matching scheme in nonlinear optics.[42-44] In the case of $\Delta n\neq0$, the phase difference between the orthogonally polarized guided modes accumulated in a transmission distance *L* is $\varphi = k_0\Delta nL$. By choosing suitable transmission distances, on-chip optical phase retardation elements such as quarter- and half-wave plates can be realized. For example, as shown in the upper/lower panel of Figure 4b, the polarization direction of the total electric field of TM_0 and TE_1 modes *E* would rotate 90 degrees anticlockwise/clockwise after a very short propagation distance about 2.6 μm (zero-order half-wave plates) in the 205/270-nm-thick

MoS_2 waveguide. This small working-distance is extremely valuable for nano-integrated polarization management applications. For these prospects to come true, interferences from the TE_0 mode and other unwanted modes had better to be eliminated. An ultimate solution is to utilize the degenerate fundamental modes in positive crystals (see **Figure S2**a in the Supporting Information for details); however, unfortunately, there is no naturally occurred positive vdW crystals known so far. As an alternative approach, we can excite the needed modes selectively using prism coupling or grating coupling methods;[45,46] in these situations, the TE_0 and other interference modes are no longer a problem.

In summary, the symmetry breaking in layered vdW crystals renders them intrinsically anisotropic in optical responses. Although hyperbolic anisotropy has been under intense studies in recent years, we demonstrate here that the elliptic anisotropy in TMDs is also highly valuable. By using MoS_2 as an example, we show the low-loss transmission of the guided modes as well as the sign- and magnitude-tunable modal birefringence. Our work represents a unique new opportunity to control the polarization behavior of photons in integrated optical circuits at the microscale, with only the thickness of the vdW materials as tuning parameter. Future research can include electrical tuning of the optical birefringence of vdW crystals (e.g. via Kerr effect), seeking for positive vdW crystals ($n_e > n_o$), and geometric designing of channel vdW waveguides, with the goal of achieving tunable modal birefringence between the fundamental (TE_0 and TM_0) guided modes.

Experimental Section

Sample preparation: Silicon wafers with a 300-nm-thick SiO_2 top layer were used as substrates for all samples. The *h*-BN and MoS_2 microcrystals of various thicknesses were exfoliated from bulk crystals.

Near-field optical measurement: The nanoimaging experiments described in the main text were performed using a commercial s-SNOM (www.neaspec.com). The s-SNOM is based on a tapping-mode AFM illuminated by monochromatic lasers of the wavelength 1530 nm. The near-field images were registered by pseudo-heterodyne interferometric detection module with tip-tapping frequency around 270 kHz, the tip-tapping amplitude is 50 nm for all experiments. By demodulating the optical signal at the third order harmonic of the tip-tapping frequency, the noise from the background and stray light can be greatly suppressed.

Supporting Information

Supporting Information is available from the Wiley Online Library or from the author.

Acknowledgments

This work was supported by the National Basic Key Research Program of China (No. 2015CB932400 and 2016YFA0202000), the National Natural Science Foundation of China (No. 11704085, 51372045, 11504063, and 11674073), and the Key Program of the Bureau of Frontier Sciences and Education Chinese Academy of Sciences (No. QYZDB-SSWSLH021).

Received: ((will be filled in by the editorial staff))
Revised: ((will be filled in by the editorial staff))
Published online: ((will be filled in by the editorial staff))

References

[1] J. D. Sarmiento-Merenguel, R. Halir, X. Le Roux, C. Alonso-Ramos, L. Vivien, P. Cheben, E. Durán-Valdeiglesias, I. Molina-Fernández, D. Marris-Morini, D. X. Xu, J. H. Schmid, S. Janz, A. Ortega-Moñux, *Optica* **2015**, *2*, 1019.

[2] S. Liao, W. Cai, J. Handsteiner, B. Liu, J. Yin, L. Zhang, D. Rauch, M. Fink, J. Ren, W. Liu, Y. Li, Q. Shen, Y. Cao, F. Li, J. Wang, Y. Huang, L. Deng, T. Xi, L. Ma, T. Hu, L. Li, N. Liu, F. Koidl, P. Wang, Y. Chen, X. Wang, M. Steindorfer, G. Kirchner, C. Lu, R. Shu, R. Ursin, T. Scheidl, C. Peng, J. Wang, A. Zeilinger, J. Pan, *Phys. Rev. Lett.* **2018**, *120*, 30501.

[3] M. Born, E. Wolf, *Principles of Optics*, Cambridge University Press, Cambridge **1999**.

[4] A. Yariv, P. Yeh, *Optical Waves in Crystals: Propagation and Control of Laser Radiation*, Wiley, Hoboken **2003**.

[5] N. Wang, X. Liu, Q. Xiong, J. Xie, S. Chen, L. Liu, *Opt. Lett.* **2017**, *42*, 2996.

[6] C. Wang, M. Zhang, X. Chen, M. Bertrand, A. Shams-Ansari, S. Chandrasekhar, P. Winzer, M. Lončar, *Nature* **2018**.

[7] Y. Zhang, Y. He, Q. Zhu, X. Jiang, X. Guo, C. Qiu, Y. Su, *Front. Optoelectron.* **2018**, *11*, 77.

[8] R. J. Black, L. Gagnon, *Optical Waveguide Modes: Polarization, Coupling and Symmetry*, McGraw-Hill, New York **2010**.

[9] J. Schollhammer, M. A. Baghban, K. Gallo, *Opt. Lett.* **2017**, *42*, 3578.

[10] D. Dai, L. Liu, S. Gao, D. Xu, S. He, *Laser Photonics Rev.* **2012**, *7*, 303.

[11] K. S. Novoselov, A. Mishchenko, A. Carvalho, A. H. Castro Neto, *Science* **2016**, *353*, 461.

[12] Y. L. W, *J. Phys. C: Solid State Phys.* **1973**, *6*, 551.

[13] S. Dai, Z. Fei, Q. Ma, A. S. Rodin, M. Wagner, A. S. McLeod, M. K. Liu, W. Gannett, W. Regan, K. Watanabe, T. Taniguchi, M. Thiemens, G. Dominguez, A. H. C. Neto, A. Zettl, F. Keilmann, P. Jarillo-Herrero, M. M. Fogler, D. N. Basov, *Science* **2014**, *343*, 1125.

[14] J. D. Caldwell, A. V. Kretinin, Y. Chen, V. Giannini, M. M. Fogler, Y. Francescato, C. T. Ellis, J. G. Tischler, C. R. Woods, A. J. Giles, M. Hong, K. Watanabe, T. Taniguchi, S. A. Maier, K.

S. Novoselov, *Nat. Commun.* **2014**, *5*, 5221.

[15] Z. Zheng, J. Chen, Y. Wang, X. Wang, X. Chen, P. Liu, J. Xu, W. Xie, H. Chen, S. Deng, N. Xu, *Adv. Mater.* **2018**, *30*, 1705318.

[16] W. Ma, P. Alonso-González, S. Li, A. Y. Nikitin, J. Yuan, J. Martín-Sánchez, J. Taboada-Gutiérrez, I. Amenabar, P. Li, S. Vélez, C. Tollan, Z. Dai, Y. Zhang, S. Sriram, K. Kalantar-Zadeh, S. Lee, R. Hillenbrand, Q. Bao, *Nature* **2018**, *562*, 557.

[17] K. Khaliji, A. Fallahi, L. Martin-Moreno, T. Low, *Phys. Rev. B* **2017**, *95*, 201401.

[18] J. S. Toll, *Phys. Rev.* **1956**, *104*, 1760.

[19] K. R. Waters, J. Mobley, J. G. Miller, *IEEE Trans. Ultrason. Ferroelectr. Freq. Control* **2005**, *52*, 822.

[20] D. N. Basov, M. M. Fogler, F. J. García De Abajo, *Science* **2016**, *354*, g1992.

[21] T. Low, A. Chaves, J. D. Caldwell, A. Kumar, N. X. Fang, P. Avouris, T. F. Heinz, F. Guinea, L. Martin-Moreno, F. Koppens, *Nat. Mater.* **2017**, *16*, 182.

[22] C. H. Perry, G. Rupprecht, R. Geick, *Phys. Rev.* **1966**, *146*, 543.

[23] M. N. Gjerding, R. Petersen, T. G. Pedersen, N. A. Mortensen, K. S. Thygesen, *Nat. Commun.* **2017**, *8*, 320.

[24] J. Son, J. Kwon, S. Kim, Y. Lv, J. Yu, J. Lee, H. Ryu, K. Watanabe, T. Taniguchi, R. Garrido-Menacho, N. Mason, E. Ertekin, P. Y. Huang, G. Lee, A. M. Van Der Zande, *Nat. Commun.* **2018**, *9*, 3988.

[25] J. Shim, S. Bae, W. Kong, D. Lee, K. Qiao, D. Nezich, Y. J. Park, R. Zhao, S. Sundaram, X. Li, H. Yeon, C. Choi, H. Kum, R. Yue, G. Zhou, Y. Ou, K. Lee, J. Moodera, X. Zhao, J. Ahn, C. Hinkle, A. Ougazzaden, J. Kim, *Science* **2018**.

[26] Q. H. Wang, K. Kalantar-Zadeh, A. Kis, J. N. Coleman, M. S. Strano, *Nat. Nanotechnol.* **2012**, *7*, 699.

[27] R. Ganatra, Q. Zhang, *ACS Nano* **2014**, *8*, 4074.

[28] S. Wang, H. Yu, H. Zhang, A. Wang, M. Zhao, Y. Chen, L. Mei, J. Wang, *Adv. Mater.* **2014**,

26, 3538.

[29] F. Yu, Q. Liu, X. Gan, M. Hu, T. Zhang, C. Li, F. Kang, M. Terrones, R. Lv, *Adv. Mater.* **2016**, *29*, 1603266.

[30] D. Hu, X. Yang, C. Li, R. Liu, Z. Yao, H. Hu, S. N. G. Corder, J. Chen, Z. Sun, M. Liu, Q. Dai, *Nat. Commun.* **2017**, *8*, 1471.

[31] G. Ghosh, *Opt. Commun.* **1999**, *163*, 95.

[32] S. Niu, G. Joe, H. Zhao, Y. Zhou, T. Orvis, H. Huyan, J. Salman, K. Mahalingam, B. Urwin, J. Wu, Y. Liu, T. E. Tiwald, S. B. Cronin, B. M. Howe, M. Mecklenburg, R. Haiges, D. J. Singh, H. Wang, M. A. Kats, J. Ravichandran, *Nat. Photonics* **2018**, *12*, 392.

[33] F. Keilmann, R. Hillenbrand, *Philos. Trans. R. Soc., A* **2004**, *362*, 787.

[34] N. Ocelic, A. Huber, R. Hillenbrand, *Appl. Phys. Lett.* **2006**, *89*, 101124.

[35] Z. Fei, A. S. Rodin, G. O. Andreev, W. Bao, A. S. McLeod, M. Wagner, L. M. Zhang, Z. Zhao, M. Thiemens, G. Dominguez, M. M. Fogler, A. H. C. Neto, C. N. Lau, F. Keilmann, D. N. Basov, *Nature* **2012**, *487*, 82.

[36] J. Chen, M. Badioli, P. Alonso-Gonzalez, S. Thongrattanasiri, F. Huth, J. Osmond, M. Spasenovic, A. Centeno, A. Pesquera, P. Godignon, A. Z. Elorza, N. Camara, D. A. F. Garcia, R. Hillenbrand, F. H. Koppens, *Nature* **2012**, *487*, 77.

[37] G. X. Ni, A. S. McLeod, Z. Sun, L. Wang, L. Xiong, K. W. Post, S. S. Sunku, B. Y. Jiang, J. Hone, C. R. Dean, M. M. Fogler, D. N. Basov, *Nature* **2018**, *557*, 530.

[38] Z. Fei, M. E. Scott, D. J. Gosztola, J. J. Foley, J. Yan, D. G. Mandrus, H. Wen, P. Zhou, D. W. Zhang, Y. Sun, J. R. Guest, S. K. Gray, W. Bao, G. P. Wiederrecht, X. Xu, *Phys. Rev. B* **2016**, *94*, 81402.

[39] J. Hu, C. R. Menyuk, *Adv. Opt. Photonics* **2009**, *1*, 58.

[40] D. M. Shyroki, A. V. Lavrinenko, *J. Opt. A: Pure Appl. Opt.* **2003**, *5*, 192.

[41] K. Kawano, T. Kitoh, *Introduction to Optical Waveguide Analysis*, John Wiley & Sons, New York **2001**.

[42] R. Normandin, G. I. Stegeman, *Opt. Lett.* **1979**, *4*, 58.

[43] T. Suhara, M. Fujimura, *Waveguide Nonlinear-Optic Devices*, Springer, New York **2003**.

[44] A. Autere, H. Jussila, Y. Dai, Y. Wang, H. Lipsanen, Z. Sun, *Adv. Mater.* **2018**, *30*, 1705963.

[45] B. M. Trabold, D. Novoa, A. Abdolvand, P. S. J. Russell, *Opt. Lett.* **2014**, *39*, 3736.

[46] W. S. Mohammed, A. Mehta, M. Pitchumani, E. G. Johnson, *IEEE Photonics Technol. Lett.* **2005**, *17*, 1441.

Supporting Information

Tunable Modal Birefringence in Low-loss van der Waals Waveguide

Debo Hu, Ke Chen, Xinzhong Chen, Xiangdong Guo, Mengkun Liu, and Qing Dai**

1. Optical nondegeneracy theorem for guide-modes in planar waveguide

In quantum mechanics, different bound states of electrons in a one-dimensional (1D) potential well are forbidden to possess the same energy level by the nondegeneracy theorem.[1] Taking the asymmetric finite 1D square potential well $V(z)$ for example (**Figure S1**a), the energy level of each electronic bound state ξ can be obtained by solving the 1D time-independent Schrödinger equation

$$\psi''(z)+\frac{2m}{\hbar^2}\left[\xi-V(z)\right]\psi(z)=0, \qquad \text{(S1)}$$

where $\psi(z)$ is the wave function corresponding to the bound states, m is the mass of the electron, and $\hbar$ is the reduced Planck constant. Shown in Figure S1b is the evolution of energy levels for eigenmodes of different order number n with respect to the potential width w, the non-crossing behaviour of these evolution curves is a clear demonstration of the energetical nondegeneracy.

Considering that the wave equation for optical waveguide and the time-independent Schrödinger equation are both Helmholtz equations which closely resemble each other, we can prove an optical analogy of the quantum nondegeneracy theorem exists, which claims different eigenmodes of a planar waveguide cannot share the same effective index of refraction.

In a planar waveguide, the photons are confined only in the z direction, which is perpendicular to the interfaces of the guiding and cladding layers. Thus, the wave equation of the transverse-electric (TE) polarized guide-modes can be written as

$$E''(z)+k_0^2\left[n^2(z)-n_{\text{eff}}^2\right]E(z)=0, \quad \text{(S2)}$$

where $E(z)$ is the electric field distribution of the guide-mode, $n(z)$ is the refractive-index profile of the waveguide, n_{eff} is the effective index of refraction for the guide-mode, and k_0 is the free-space

wavenumber. To prove the optical nondegeneracy theorem we start by assuming that the opposite proposition is true, i.e. there are two different yet linearly independent solutions of **Equation S2**, E_1 and E_2, share the same eigenvalue n_{eff}. By substituting E_1 and E_2 into Equation S2 and rearranging the equations, we have

$$E_1'' / E_1 = k_0^2 \left[n_{\text{eff}}^2 - n^2(z) \right] = E_2'' / E_2, \qquad \text{(S3)}$$

which can be further manipulated as

$$E_1'' E_2 - E_1 E_2'' = \left(E_1' E_2 - E_1 E_2' \right)' = 0. \qquad \text{(S4)}$$

Equation S4 implies

$$E_1' E_2 - E_1 E_2' = c, \qquad \text{(S5)}$$

where c is a constant. Since E_1 and E_2 are both associated with confined waveguide eigenmodes, they must vanish at infinity; as a result, c must be zero. This means

$$E_1' / E_1 = E_2' / E_2. \qquad \text{(S6)}$$

Integrating **Equation S6** from both sides we have

$$\ln E_1 = \ln E_2 + \ln C, \quad \text{(S7)}$$

where C is another integration constant. **Equation S7** implies that E_1 and E_2 are linearly dependent

$$E_1 = C E_2, \qquad \text{(S8)}$$

this is in direct contradiction with the initial assumption thus concludes the proof. The nondegeneracy of the transverse-magnetic (TM) polarized guide-modes as well as that of guide-modes with different polarization states can be proved following the same procedure described above.

This optical nondegeneracy theorem can be further verified by using graphical illustration. Shown in Figure S1c is the schematic of an asymmetric Air-Si-SiO_2 three-layer waveguide. The refractive indices for its superstrate, substrate and guiding layers are n_1, n_2 and n_0, respectively ($n_0 > n_2 > n_1$); and the guiding layer thickness is d. By imposing the electromagnetic boundary conditions upon Equation 2 at both interfaces of the waveguide we can relate the structural and optical parameters of the

waveguide with the effective refractive indices of the guide-modes n_{eff} explicitly, via the so-called characteristic equations. The characteristic equations for the transverse electric (TE) and transverse magnetic (TM) polarized guide-modes can be written as[2]

$$k_0\sqrt{n_0^2-n_{\text{eff,TE}}^2}\,d=\tan^{-1}\left(\frac{\sqrt{n_{\text{eff,TE}}^2-n_1^2}}{\sqrt{n_0^2-n_{\text{eff,TE}}^2}}\right)+\tan^{-1}\left(\frac{\sqrt{n_{\text{eff,TE}}^2-n_2^2}}{\sqrt{n_0^2-n_{\text{eff,TE}}^2}}\right)+p\pi \quad \text{(S9)}$$

and

$$k_0\sqrt{n_0^2-n_{\text{eff,TM}}^2}\,d=\tan^{-1}\left(\frac{n_0^2}{n_1^2}\frac{\sqrt{n_{\text{eff,TM}}^2-n_1^2}}{\sqrt{n_0^2-n_{\text{eff,TM}}^2}}\right)+\tan^{-1}\left(\frac{n_0^2}{n_2^2}\frac{\sqrt{n_{\text{eff,TM}}^2-n_2^2}}{\sqrt{n_0^2-n_{\text{eff,TM}}^2}}\right)+q\pi \quad \text{(S10)}$$

respectively. In **Equation S9** and **S10**, p and q are the order numbers of TE and TM polarized eigenmodes, respectively.

Shown in Figure S1d are the thickness dispersions of eigenmodes in the planar waveguide, obtained by solving Equation S9 and S10 numerically. In the limit as d approaches the cut-off thickness of each guide-mode, n_{eff} of the relevant mode approaches the substrate refractive index n_2, corresponding to the critical state that the photons are about to leak out of the guiding layer and propagate freely in the substrate; In the limit as d approaches infinity, n_{eff}'s of all the guide-modes approach the guiding layer refractive index asymptotically, corresponding to the situation that the photons propagate freely in a bulk material of refractive index n_0. Besides these two extreme situations, the dispersion curves of different eigenmodes never intersect with each other. Therefore, for a waveguide with a definite guiding layer thickness, its different eigenmodes cannot possess the same effective index of refraction. The same non-crossing behaviour of the dispersion curves in Figure S1d as that manifested in Figure S1b is a piece of convincing evidence for the validity of the optical nondegeneracy theorem.

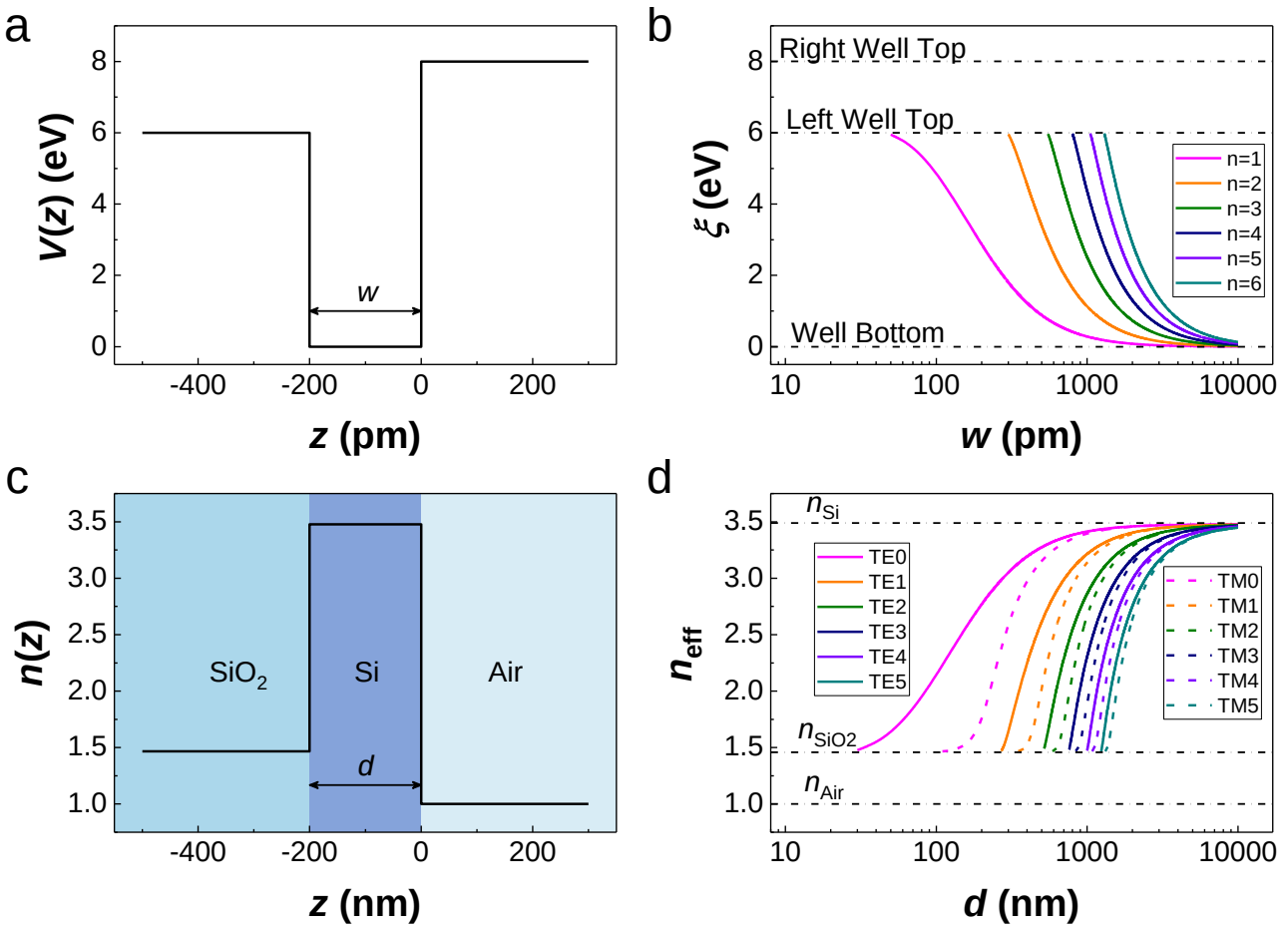

Figure S1. Nondegeneracy of eigenmodes in 1D potential well and planar waveguide. a) Asymmetric finite 1D square potential well $V(z)$ for electrons. b) Energy level evolution of different bound electron eigenmodes in the potential well illustrated in a with respect to the potential width, obtained by solving **Equation S1** numerically, n is the mode order. c) Refractive-index profile $n(z)$ of the Air-Si-SiO_2 three-layer waveguide. d) Thickness dispersions of TE and TM polarized eigenmodes in the planar waveguide illustrated in c.

2. Anisotropy-induced nondegeneracy violation in van der Waals waveguide

In quantum mechanics, the nondegeneracy theorem can be violated by introducing singularities into the 1D potential;[3-5] however, the corresponding refractive-index profiles containing singularities cannot be realistically established in the real optical system, new strategy is necessary to circumvent the optical nondegeneracy theorem.

Since the TE and TM guide-modes are orthogonally polarized, their respective electric field components experience different components of the refractive-index tensors. In a planar waveguide made of exclusively isotropic materials, the optical nondegeneracy theorem always holds; however,

if anisotropic materials are introduced into the waveguide, the refractive-index profile would split, and this provides us with the possibility to defy the optical nondegeneracy theorem.

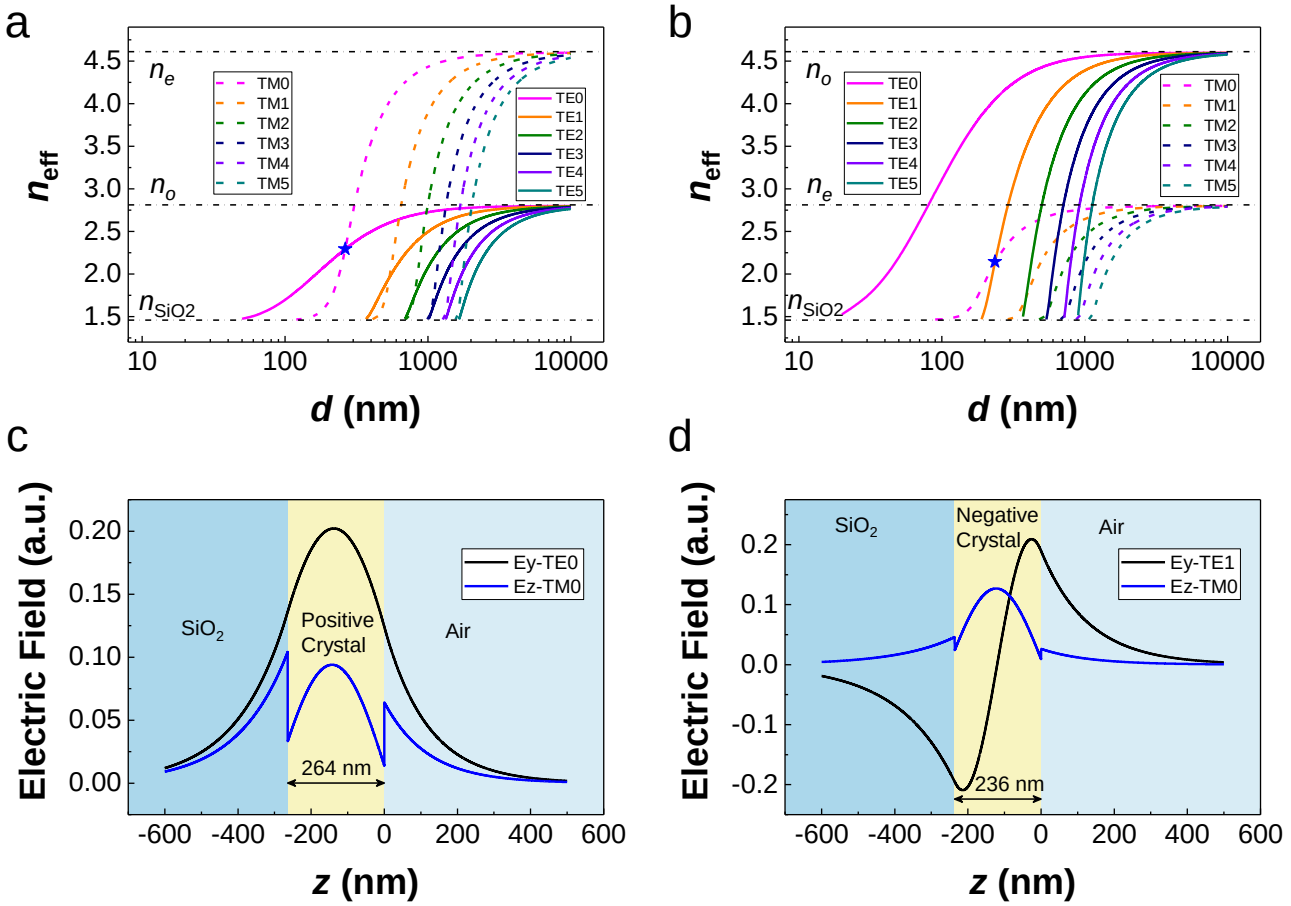

Figure S2. Anisotropy-induced optical degeneracy of eigenmodes in planar waveguides with uniaxially anisotropic guiding layers. a)-b) Thickness dispersions of ordinary and extraordinary eigenmodes in planar waveguide with positively and negatively anisotropic guiding layer, respectively. c)-d) Electric field distributions of degenerate eigenmodes indicated in a and b by the blue stars, respectively.

Shown in **Figure S2**a and Figure S2b are the thickness dispersions of the eigenmodes in a planar waveguide with a positively and negatively anisotropic guiding layer, respectively, obtained by solving **Equation 2** and **3** in the main text numerically. There are two intriguing features in both Figure S2a and Figure S2b: the grouping yet non-crossing of guide-modes with the same polarization state, and the crossing of guide-modes with different polarization states. Specifically, in the case of a positive guiding layer, as d approaches infinity, n_{eff}'s for the TM (TE) polarized extraordinary (ordinary) eigenmodes approach asymptotically to the value of n_e (n_o). Since $n_e > n_o$ for a positive guiding layer, there are always intersection points for the thickness dispersion curves of the TE and

TM polarized modes with the same order number; the *l*th order TE mode intersects with all the TM modes of the order number ≥*l*. In the case of a negative guiding layer, by the same argument, the *l*th order TM mode intersects with all the TE modes of the order number ≥*l*+1; however, none dispersion curves of the TM modes intersect with that of the fundamental TE mode. At these intersection points (like the ones indicated by blue stars), although the two crossed guide-modes are of different electric field distributions as shown in Figure S2c and Figure S2d, they share the same effective refractive index. Therefore, the optical nondegeneracy theorem can be violated in a well-designed anisotropic waveguide.

3. Modal birefringence tunability of air-Si-SiO_2 waveguide

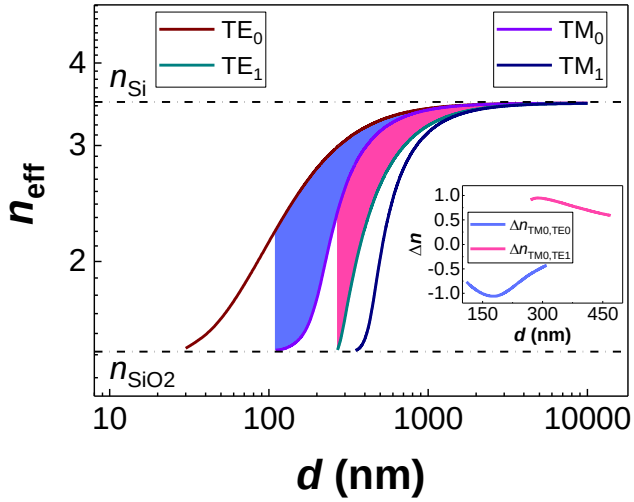

Figure S3. Thickness dispersions of TE and TM polarized modes in air-Si-SiO_2 three-layer waveguide. There is no intersection point between dispersion curves of different modes, accordingly, the modal birefringences can only be tuned in magnitude in limited ranges and usually display non-monotonicity with respect to the guiding layer thickness as shown in the inset.

4. Near-field images of MoS_2 microcrystals with different thicknesses

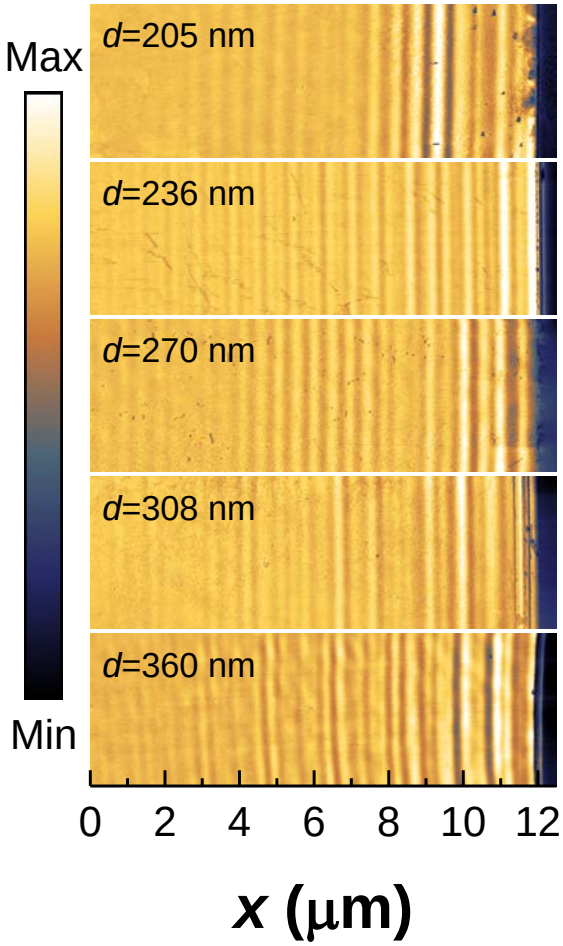

Figure S4. Near-field images of MoS_2 microcrystals with different thicknesses

References

[1] L. D. Landau, E. M. Lifshitz, *Quantum Mechanics*, Pergamon Press, Oxford **1977**.

[2] K. Kawano, T. Kitoh, *Introduction to Optical Waveguide Analysis*, John Wiley & Sons, New York **2001**.

[3] R. Loudon, *Am. J. Phys.* **1959**, *27*, 649.

[4] S. Kar, R. R. Parwani, *EPL* **2007**, *80*, 30004.

[5] R. Loudon, *Proc. R. Soc. A* **2016**, *472*.